Research Article
Vol. 26, No. 23 | 12 Nov 2018 | OPTICS EXPRESS 30231
Optics EXPRESS

Spatial resolution improvement for an optical transition radiation monitor by asymmetric light collection

A. POTYLITSYN,[1,*] L. SUKHIKH,[1] G. KUBE,[2] AND A. NOVOKSHONOV[1,2]

[1]Tomsk Polytechnic University, 30, Lenin St., Tomsk, 634050, Russia
[2]Deutsches Elektronen-Synchrotron (DESY), Hamburg, Germany
[*]potylitsyn@tpu.ru

Abstract: The applicability of optical transition radiation (OTR) for measurements of micron sized transverse electron beam profiles is limited not only by the optical system resolution which has a fundamental limit imposed by the uncertainty principle. In the case of OTR generation, a single electron crossing the boundary between vacuum and screen cannot be considered as a single emitting point with isotropic angular distribution. On the contrary, the radiation is emitted from an area with a transverse range that is defined by the radial extension of the electron's Lorentz contracted Coulomb field and is typically estimated as $\gamma\lambda$ (with γ the Lorentz factor and λ the wavelength of observation). The OTR angular distribution has a characteristic "funnel" shape. As a result the one-dimensional image of a single electron measured with an ideal thin lens has a double lobe shape, and the resolution of any OTR based imaging system is determined by this double lobe function which is also known as OTR Point Spread Function (PSF). As a consequence, the reconstruction of micron sized electron beam profiles is hampered not only due to the fundamental diffraction limit, but also due to the PSF lobe shape. In this paper we present two approaches to improve the spatial resolution of an OTR monitor based on asymmetric light collection using a traditional optical system which allows blocking of one of the lobes. With such a scheme, an OTR PSF can be achieved that is comparable to the one of an ideal point source (Airy distribution).

1. Introduction

Transverse beam profile diagnostics based on optical transition radiation (OTR) is a routine technique at most modern electron linear accelerators (linacs) [1–3]. The mechanism of OTR generation possesses a practically prompt response ($\Delta t \sim h/\Delta E$, $\Delta E \sim 1$ eV, $\Delta t \sim 10^{-15}$ s) and a linear dependency on the initial beam intensity, neglecting coherent radiation emission effects driven by the microwave instability which is sometimes observed at modern linac based Free-Electron-Lasers (FELs) [4,5]. For electron accelerators with energies higher than 50 MeV for instance, the intensity of the OTR light collected by an optical system with a numerical aperture of ~0.1 rad can achieve $\sim 10^{-3}$ photons/electron, assuming an optical filter with relative bandwidth of $\Delta\lambda/\lambda \sim 5\,\%$.

The spatial resolution of a transverse beam size monitor based on OTR is determined by the so-called Point Spread Function (PSF) or, in other words, by the response of the monitor optical system to a point charge crossing the target. With knowledge of the PSF, in principle it is possible to reconstruct beam size and beam shape from an electron bunch passing through the target applying a deconvolution algorithm to the measured OTR image.

In the first approximation for $E > 100$ MeV the PSF can be obtained based on approximations of classical optics. In this approach the field of a relativistic point charge is considered as a set of the electromagnetic waves (the pseudo photon approximation) see, for example [6–9].

#337823 https://doi.org/10.1364/OE.26.030231
Journal © 2018 Received 18 Jul 2018; revised 1 Oct 2018; accepted 15 Oct 2018; published 2 Nov 2018

Optics EXPRESS

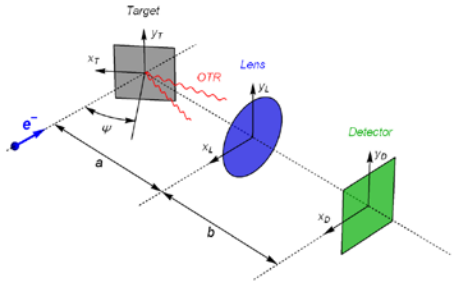

Fig. 1. Optical scheme of OTR beam size monitor.

A typical sketch illustrating the observation geometry of backward OTR is presented in Fig. 1. The generation of backward OTR is considered from a target with ideal conductivity according to [9]

$$\frac{dW}{\hbar d\omega d\Omega} = \frac{\alpha}{\pi^2}\frac{\theta_x^2+\theta_y^2}{\left(\gamma^{-2}+\theta_x^2+\theta_y^2\right)^2}, \tag{1}$$

where ω is the frequency of the emitted photons, γ is the Lorentz-factor, θ_x, θ_y are the projection angles with respect to the specular reflection direction, $\hbar$ is the Planck constant, and α is the fine structure constant. It should be mentioned that formula (1) is valid for the ultra-relativistic case and for the far-field zone only.

As it was shown in [10,11], for distances $a < \gamma^2\lambda$ away from the target (λ is the wavelength of the emitted OTR photon), the angular distribution of OTR is affected by the transverse size of the particle Coulomb field which is in the order of $\sim \gamma\lambda$ and which induces polarization currents at the target surface in a region with radius $\gamma\lambda$ (so-called the prewave zone effect). As consequence the OTR angular distribution is broadened and depends on the ratio $R = a/\gamma^2\lambda$. However, in the case of OTR imaging where the detector is placed in the image plane, the pre-wave zone effect can be neglected for arbitrary ratios R [6–8]. While simulations of OTR diagnostic techniques were recently performed using the Zemax code [12], the approach which is presented in the following is based on classical diffraction theory where the electromagnetic field of the point charge is considered as a set of transverse electromagnetic waves.

Such a simple approach allows to obtain general features of the OTR images and compare them for different wavelengths, apertures, electron energies, etc. Zemax's simulations can be used effectively for taking into account characteristics of the optical system, defocusing effects and so on after choosing of the experimental scheme which can be done on the classical diffraction model.

2. Model for OTR PSF calculation

Under ultra-relativistic approximation the particle Coulomb field can be sufficiently described by its transverse components and it is possible to write down the OTR field in the lens plane in analogy with wave scattering at a finite size conducting screen:

$$E_{x,y}^{L}(\mathrm{X}_L,\mathrm{Y}_L) = \mathrm{const}\int_{S_T} d\mathrm{X}_T d\mathrm{Y}_T \begin{Bmatrix}\cos\varphi_T\\ \sin\varphi_T\end{Bmatrix} K_1\left(\frac{k}{\beta\gamma}R_T\right)\times$$
$$\exp\left[i\frac{k}{2a}\left(\mathrm{X}_T^2+\mathrm{Y}_T^2\right)\right]\exp\left[-i\frac{k}{a}\left(\mathrm{X}_L\mathrm{X}_T+\mathrm{Y}_T\mathrm{Y}_L\right)\right]. \tag{2}$$

Optics EXPRESS

Here $R_T = \sqrt{\mathrm{X}_T^2 + \mathrm{Y}_T^2}$, $(\mathrm{X}_T,\ \mathrm{Y}_T)$ and $(\mathrm{X}_L, \mathrm{Y}_L)$ are the coordinates of target surface and lens plane, S_T is the target surface area, $\begin{Bmatrix}\cos\varphi_T \\ \sin\varphi_T\end{Bmatrix} = \dfrac{1}{\sqrt{\mathrm{X}_T^2 + \mathrm{Y}_T^2}}\begin{Bmatrix}\mathrm{X}_T \\ \mathrm{Y}_T\end{Bmatrix}$, $K_1(x)$ is the MacDonald function of the first order, and $k = 2\pi/\lambda$. For a transverse target size which is much larger than the field radius $\gamma\lambda$ it is possible to extend the integration region over the target surface to infinity.

The OTR fields in the image plane using thin lens approximation can be written in the following way [7,8]:

$$E_{x,y}^{D}(\mathrm{X}_D, \mathrm{Y}_D) = \mathrm{const}\int\limits_{S_L} d\mathrm{X}_L d\mathrm{Y}_L E_{X,Y}^{L}(\mathrm{X}_L, \mathrm{Y}_L)\times\exp\left[-i\frac{k}{b}\left(\mathrm{X}_L\mathrm{X}_D + \mathrm{Y}_L\mathrm{Y}_D\right)\right]. \quad (3)$$

Here the integration is performed over the lens aperture $\mathrm{S_L}$. For the sake of simplicity dimensionless variables are introduced in the following:

$$\begin{Bmatrix}x_T \\ y_T\end{Bmatrix} = \frac{2\pi}{\gamma\lambda}\begin{Bmatrix}\mathrm{X}_T \\ \mathrm{Y}_T\end{Bmatrix},\ \begin{Bmatrix}x_L \\ y_L\end{Bmatrix} = \frac{\gamma}{a}\begin{Bmatrix}\mathrm{X}_L \\ \mathrm{Y}_L\end{Bmatrix},\ \begin{Bmatrix}x_D \\ y_D\end{Bmatrix} = \frac{2\pi}{\gamma\lambda}\begin{Bmatrix}\mathrm{X}_D \\ \mathrm{Y}_D\end{Bmatrix}. \quad (4)$$

Inserting Eq. (2) in Eq. (3) and taking into account the variable substitution, the following 4-fold integration has to be solved:

$$\begin{Bmatrix}E_x^D(x_D, y_D) \\ E_y^D(x_D, y_D)\end{Bmatrix} = \mathrm{const}\int dx_T dy_T \int\limits_{S_T} dx_L dy_L \int\limits_{S_L}\begin{Bmatrix}x_T \\ y_T\end{Bmatrix}\frac{K_1\left(\sqrt{x_T^2 + y_T^2}\right)}{\sqrt{x_T^2 + y_T^2}}\times$$
$$\exp\left[i\left(x_T x_L + x_T y_L\right)\right]\cdot\exp\left[-\frac{i}{\mathrm{M}}\left(x_L x_D + y_L y_D\right)\right]\cdot\exp\left[i\frac{x_T^2 + \mathrm{y}_T^2}{4\pi R}\right]. \quad (5)$$

$M = b/a$ is the optical system magnification (in the following all simulations will be carried out for the case $M = 1$, i.e. $a = b$). The condition of ideal focusing was used in order to obtain Eq. (5):

$$1/a + 1/b = 1/f. \quad (6)$$

For geometries with azimuthal symmetry the radial component of the OTR field in the image plane can be reduced to a more simple expression, see [7,8]:

$$E_D(r_D) = \int\limits_0^{r_{T\max}} r_T dr_T K_1(r_T) G(r_T, r_D, r_m)\exp\left[i\frac{r_T^2}{4\pi R}\right],$$
$$G\left(r_T, r_D, r_L^{\max}\right) = \int\limits_0^{r_L^{\max}} r_L dr_L J_1\left(r_T r_L\right) J_1\left(r_L r_D\right) = \quad (7)$$
$$\frac{r_L^{\max}}{r_D^2 - r_T^2}\left[r_T J_0\left(r_L^{\max} r_T\right) J_1\left(r_L^{\max} r_D\right) - r_D J_0\left(r_L^{\max} r_D\right) J_1\left(r_L^{\max} r_T\right)\right].$$

A spatial resolving detector located in the image plane will measure a two-dimensional distribution which is proportional to the intensity of OTR. Therefore, the OTR PSF under assumption of target ideal reflectivity can be can be finally written as

Optics EXPRESS

$$\frac{d^2W}{\hbar d\omega d\Omega} = \text{const}\left(\left|E_x^D\right|^2 + \left|E_y^D\right|^2\right) = \text{const}\left(\frac{d^2W_x^D}{\hbar d\omega d\Omega} + \frac{d^2W_y^D}{\hbar d\omega d\Omega}\right) = \text{const}\left|E_D\left(r_d\right)\right|^2 . \quad (8)$$

3. OTR imaging

Measurements of OTR images using a conventional optical system as depicted in Fig. 1 allow avoiding the influence of the pre-wave zone effect [7,8]. The spatial resolution of such a scheme is determined by the lens aperture and by the wavelength of observation and can be characterized by the PSF. Results of radial PSF distribution calculations according to Eqs. (7) and (8) are shown in Fig. 2(a). The calculation parameters are as follows: $R = 1$; $\gamma = 1000$; $r_L^{\max} = 200$ ($\theta_{\max} = 0.2$ rad) for the blue curve and $r_L^{\max} = 100$ ($\theta_{\max} = 0.1$ rad) for the red curve. The lens diameter for the latter case, for instance, is defined as $d_L = 2a\, r_L^{\max} / \gamma$ ($d_L = 100$ mm for $a = 500$ mm).

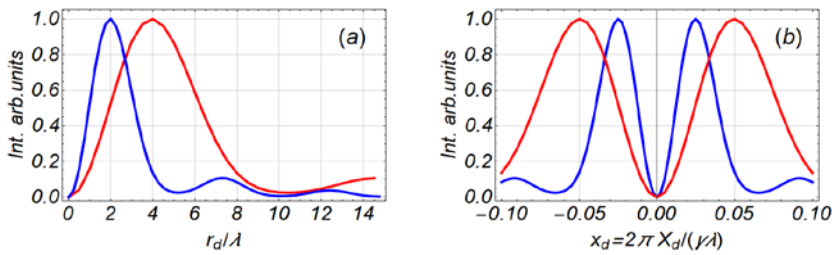

Fig. 2. (a) Radial distributions of OTR images calculated in near-field approximation (R = 1; $\gamma = 1000$; $\lambda = 0.5$ um; a = 500 mm; M = 1; d_L = 200 mm (blue curve) and d_L = 100 mm (red curve)). (b) PSF distributions calculated for $y_d = 0$ for the same conditions as function of the dimensionless coordinate x_d.

Equations (7) and (8) are written in the universal form with dimensionless variables. Therefore, the same plots presented in Fig. 2(b) describe also the PSF for particles with $\gamma = 2000$ and $\theta_{\max} = 0.1\left(r_L^{\max} = \gamma\theta_{\max}\right)$ (blue curve). As a rule, an experimental scheme can include a polarizer which may select either the x- or the y-field component. In order to calculate the OTR image in this case, it is sufficient to select only one term in Eq. (8). In the following all calculations of OTR images will be performed for the horizontal polarization component only based on Eq. (5) for the same parameter set as used in Fig. 2(b).

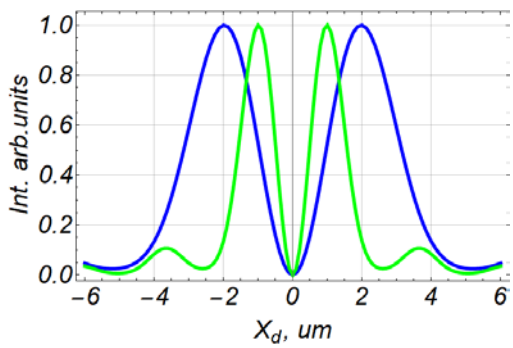

Fig. 3. PSF distributions for horizontal polarization component calculated using the far-field approximation ($y_d = 0$; $R \to \infty$; $\gamma = 2000$; $\lambda = 0.5$ um; a = 500 mm; M = 1; $d_L = 100$ mm (green curve), $d_L = 50$ mm (blue curve)).

Figure 3 shows the one-dimensional horizontal PSF distribution. In order to calculate the OTR image from a beam with Gaussian transverse profile, this PSF can be approximated by a simple analytical function

$$f_1(X_D) = q_0 X_D^2 \exp\left[-X_D^2 / q_1^2\right], \tag{9}$$

with q_0, q_1 being free fit parameters [13]. While q_0 is a simple amplitude factor, the parameter q_1 characterizes the PSF and can be used to give a resolution estimate as will be shown below. The result of the convolution of a Gaussian beam profile with rms size σ and the PSF according to Eq. (9) can be expressed by the following analytical function [13]:

$$F_{\text{conv}}(\mathrm{X}_D, \sigma) = \frac{q_0 q_1^2}{\sigma} \frac{1}{\sqrt{2/q_1^2 + 1/\sigma^2}} \frac{2\sigma^4 + q_1^2\left(\sigma^2 + \mathrm{X}_D^2\right)}{\left(q_1^2 + 2\sigma^2\right)^2} \exp\left[-\frac{\mathrm{X}_D^2}{\left(q_1^2 + 2\sigma^2\right)}\right]. \tag{10}$$

Figure 4a presents a calculated PSF for the following parameter set

$$\begin{aligned} &\gamma = 2000; \lambda = 500\,\text{nm}; a = b = 500\,\text{mm}; f = 250\,\text{mm}; \\ &d_{\text{L}} = 100\,\text{mm}\ (\theta_m = 0.1). \end{aligned} \tag{11}$$

The calculated function was fitted with the fit function Eq. (9), resulting in $q_1 = 2.0\,\text{um}$. As can be seen, there is a good agreement especially in the central part between the fit and the PSF calculation based on Eq. (5). In order to illustrate the sensitivity of an OTR based beam profile measurement on the PSF influence, the PSF distribution from Fig. 4a was convoluted with Gaussian beams with sizes $\sigma =$ 0.5; 1.0; 2; 4 um according to Eq. (10). The results are plotted in Fig. 4(b). As can be seen, for beam sizes $\sigma < q_1$ the profiles exhibit a two-lobe structure. For this case (so called PSF dominated regime) the problem of reconstructing the initial beam profile is rather complicated, see [12,13]. Only in the case $\sigma > 10q_1$ the PSF influence is so small that fitting the convoluted data with a Gaussian function results in a rms beam size which practically coincides with the input size for the beam [13].

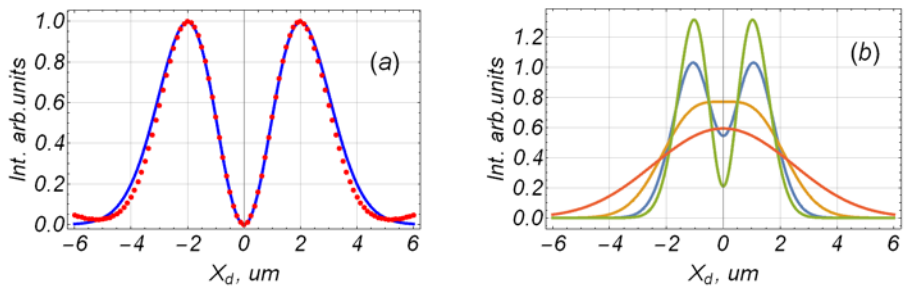

Fig. 4. (a) Horizontal PSF distribution (points) and fit for $q_1 = 2,0$ um (see Eq. (9), solid curve) calculated for the same conditions as before ($d_L = 100$ mm). (b) Beam images calculated with the PSF from Fig. 4(a) for different rms beam sizes (green line – $\sigma = 0.5$ um; blue line – $\sigma = 1$ um; yellow line – $\sigma = 2$ um; red line – $\sigma = 4$ um.

4. Methods to improve the OTR spatial resolution for beam imaging

The author of [8] proposed to use the parameter $R_{i0} \approx 1.12\,\lambda/\theta_m$ for the characterization of the resolution (for a magnification of $M = 1$ which is the case throughout this publication). Thus, the spatial resolution depends on the wavelength λ and on the lens acceptance θ_m.

One possible ways to improve the spatial resolution was proposed in [6,14]. The authors proposed to shield the central part of the lens aperture by a mask which is placed just in front of the lens. The shielding effect results in a suppression of the PSF side lobes at larger distances such that only a double lobe structure remains. In [8] a criterion was proposed for the optimal choice of the mask aperture:

$$\theta_{\text{mask}} = 0.2779\,\theta_m^{\text{lens}} \tag{12}$$

Figure 5 presents calculated PSFs taking into account the influence of the shielding mask. The optimal mask effect is shown by the green curve (see Fig. 5). Despite a decrease of the OTR yield, the oscillatory behavior in the distribution tails (i.e. the region where the PSF is in the range $|X_D| > 2q_1$) is suppressed. Evidently, the volcano-like part of the OTR distribution in the lens plane is transformed into a two-lobe shape as before.

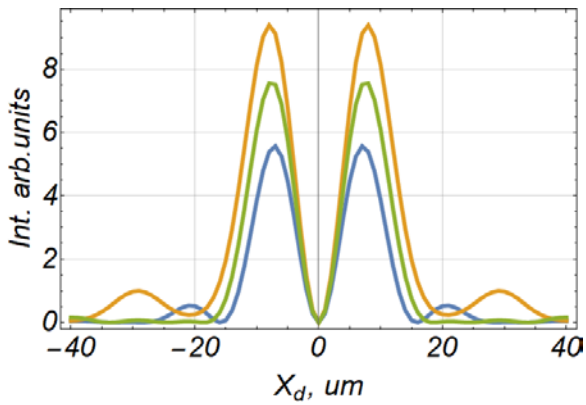

Fig. 5. Calculated horizontal PSF distributions for the same parameter set as before, taking into account the influence of the shielding mask ($d_L = 50$ mm, yellow line – no mask; green line – $d_{mask} / d_L = 0.28$; blue line – $d_{mask} / d_L = 0.4$).

As was noticed in [8] "… the effect of the mask can be interpreted as increasing the uncertainty in the momentum for to reduce the uncertainty in the position …". In the course of the preceding work two methods are proposed by which the OTR PSF contribution can further be reduced close to the level of the Airy function which represents the ultimate resolution level of a point source.

Basis of the first method is the installation of a mask in front of the lens with appropriate size at a position which is asymmetric with respect to the optical axis. If mask size and position are selected in a proper way it is possible to block one of the lobes of the horizontal angular OTR distribution. In this case information is extracted only from the second lobe in the lens plane or in the $k_x - k_y$ phase space. Due to the properties of the Fourier transformation the output in the $X_D - Y_D$ plane (i.e. the detector plane) will also have a single maximum distribution.

Figures 6 and 7 represent the evolution of the OTR PSF as function of the mask position using the horizontally polarized radiation component. As expected, in the case of full blocking of one of the lobes in the lens plane (Fig. 6(f)), the resulting PSF possesses a single maximum only (Fig. 7(f)). In all cases under consideration, the PSF distributions were calculated based on Eq. (13) which is the far-field zone approximation for the radiation field, using a lower limit for the integration over X_L as indicated in Fig. 6(b):

Optics EXPRESS

$$E_x^D\left(x_D, y_D\right) = \int_{x_{L\min}}^{r_L^{\max}} dx_L \int_{y_{L\min}}^{y_{L\max}} \frac{dy_L x_L}{\sqrt{x_L^2 + y_L^2}} \frac{\exp\left\{-\left(x_L x_D + y_L y_D\right)\right\}}{\left(1 + x_L^2 + y_L^2\right)}, \tag{13}$$

where

$$y_{L\min} = -\sqrt{\left(r_L^{\max}\right)^2 - x_L^2}, \; y_{L\max} = -\sqrt{\left(r_L^{\max}\right)^2 - x^2{}_L}. \tag{14}$$

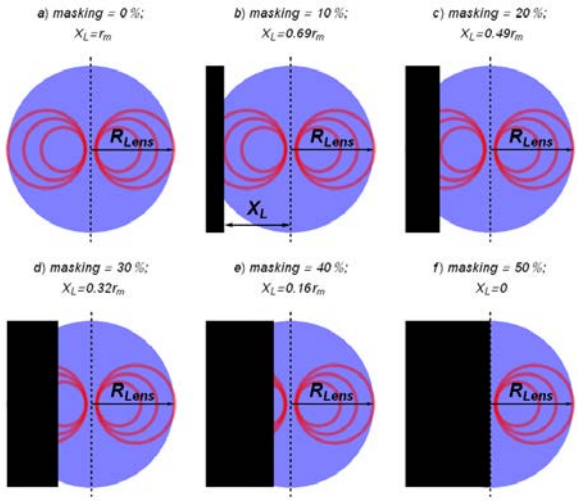

Fig. 6. Scheme of the lens screening by an asymmetric mask. The red contour plot illustrates schematically the lobe structure of the horizontally polarized OTR intensity.

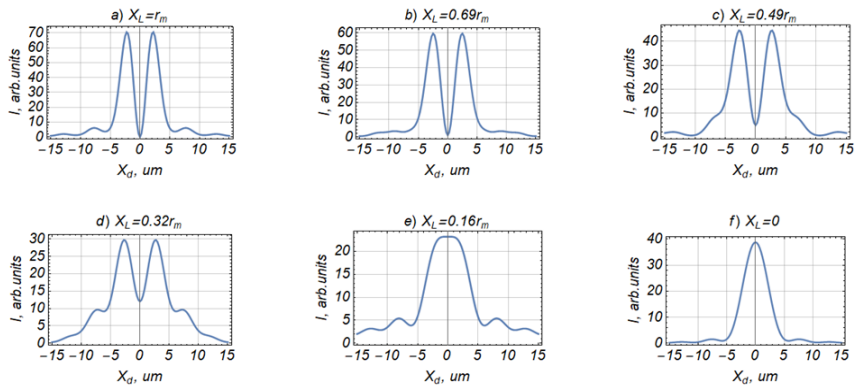

Fig. 7. PSF distributions calculated for the lens screening schematically shown in Fig. 6.

The single maximum PSF in this case can be approximated by a Gaussian distribution as shown in Fig. 8. For the parameters considered before (a = 500 mm, $\lambda = 0.5$ μm, M = 1, $\theta_m = 0.1$ rad) the rms size of this PSF is much smaller than the parameter R_{i0}: $\sigma = 2.01\,\text{um} < 1.12\,\lambda/\theta_m = 5.6$ um, but the radius corresponding the first minimum in the PSF distribution $R_{1PSF} = 5.75\,\text{um}$, practically coincides with R_{i0}.

Optics EXPRESS

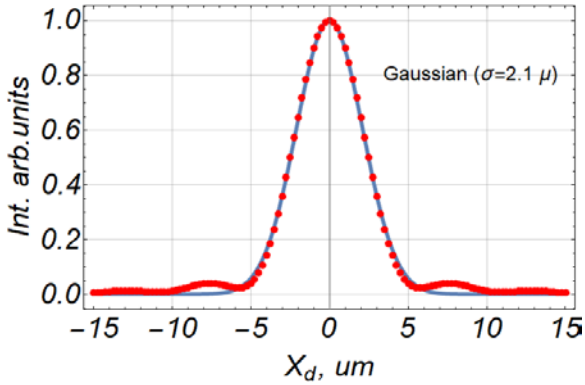

Fig. 8. Gaussian fit using the PSF for the case shown in Fig. 6(f) (c.f. also Fig. 7(f)).

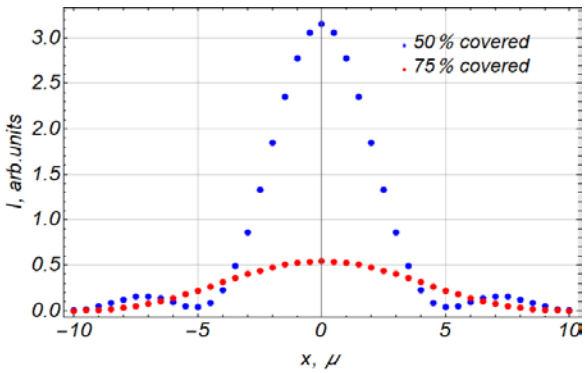

Fig. 9. Comparison of PSF distributions for masking with different asymmetric masks (blue – 50% screening, red – 75% screening).

In Fig. 9 a PSF comparison is shown for two cases, using masking of 75% and of 50% (i.e. the case shown in Figs. 6 and 7(f)) of the lens aperture. As can be seen, with increasing screening the PSF is broadened. Again this effect is connected with the uncertainty principle because the narrowing of the distribution in the $k_x - k_y$ phase space results in a broadening of *x-y* distribution.

The second method to improve the spatial resolution of an OTR monitor has the same purpose to create a PSF with a single maximum. Again, the OTR horizontal polarization component will be considered in the following. However, in this case the idea is to displace the imaging lens asymmetrically as depicted in Figs. 10 and 11.

Optics EXPRESS

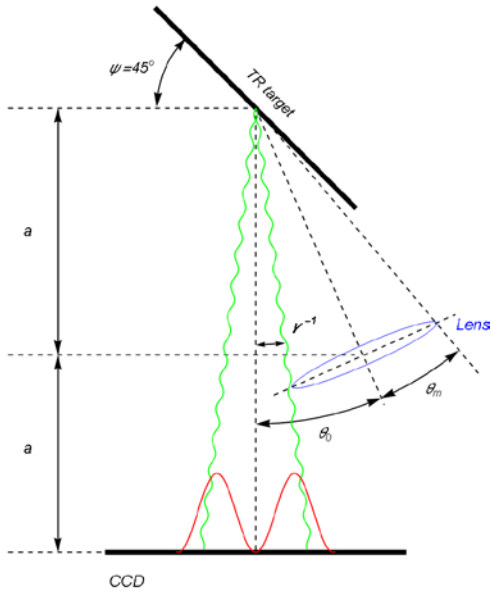

Fig. 10. Scheme of the asymmetric lens displacement.

If the lens optical axis is disoriented with respect to the specular reflection direction from the OTR target at an angle of θ_0 with $\theta_0 - \theta_m >> \gamma^{-1}$ as shown in Fig. 10, the OTR light will be collected from the outside region of the OTR lobe-shape distribution, c.f. Figure 11.

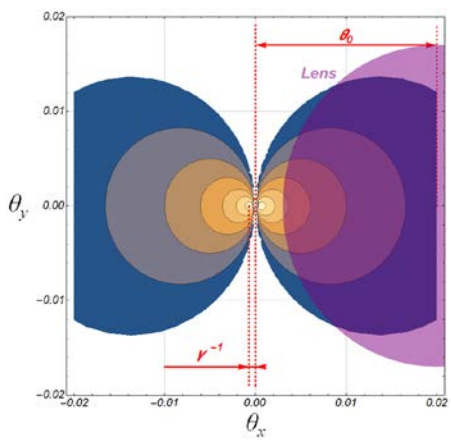

Fig. 11. Scheme of the asymmetric light collection.

Evidently, for such imaging geometry the part of the horizontal OTR distribution which is accepted by the lens possesses only a single maximum. The PSF calculation for this asymmetric light collection geometry is based on Eq. (5). The integration over the lens aperture is carried out under the restriction

$$\left(x_L - x_{0L}\right)^2 + \left(y_L - y_{0L}\right)^2 \le r_{lens}^m, \tag{15}$$

where

$$x_{0L} = \gamma\Delta\theta_{0x}; y_{0L} = \gamma\Delta\theta_{0y}; r_{lens}^m = \gamma / a\, R_{lens}. \tag{16}$$

Results of such PSF calculations using asymmetric light collection geometries are presented in Fig. 12 for $\theta_m = 100/\gamma = 0.1\,\text{rad}$ (green points) and $\theta = 50/\gamma = 0.05\,\text{rad}$ (red points). The remaining parameters for the calculation are the same as before.

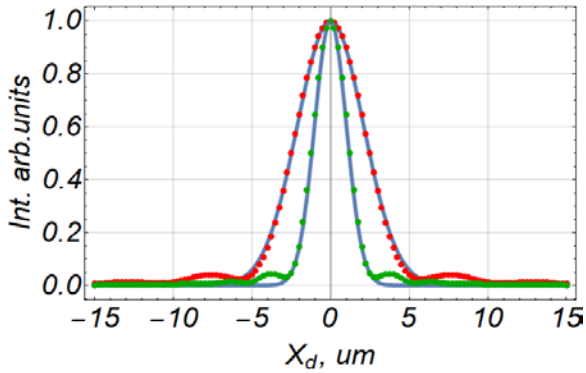

Fig. 12. Calculated PSF distributions for an asymmetric lens aperture (red points $\theta_{0x} = 60/\gamma$; $\theta_{0y} = 0$; $\theta_m = 50/\gamma$ – red points); $\theta_{0x} = 110/\gamma$, $\theta_m = 100/\gamma$ (green points) and Gaussian fits for them.

Approximating the central maximum by a Gaussian distribution results in an rms value of $\sigma_1 = 1.01$ um for the first case and $\sigma_2 = 2.02$ um for the second one (see Fig. 12).

5. Discussion

In the present report it was shown that an asymmetric mask in front of the imaging lens or an asymmetric light collection geometry caused by a displacement of the imaging lens both result in light collection from only one lobe of a linearly polarized OTR intensity distribution. As consequence, the PSF possesses also a single maximum in the image plane. In contrast to that, the previously proposed scheme for resolution improvement based on a mask which is oriented coaxially with the lens results in a two-lobe PSF structure with suppression of the outer maxima [8].

In the following PSF distributions calculated for asymmetric OTR light collection (see Fig. 8 and Fig. 12) will be compared with the well-known Airy distribution, describing the PSF of an isotropic emitting point source [15]. It is expressed as

$$AF(R_D) = (I_1(\alpha R_D)/\alpha R_D)^2, \tag{17}$$

with $I_2(x)$ the first order Bessel function, where

$$\alpha = 2\pi\theta_m/\lambda,\ \alpha = 2\pi\theta_m/\lambda,\ R_D = \sqrt{\mathrm{X}_D^2 + \mathrm{Y}_D^2}. \tag{18}$$

In Fig. 13 the results of a calculation for $\lambda = 0.5$ μm, $\theta_m = 0.1$ and $\mathrm{Y_D} = 0$ are shown. The first minimum of the Airy function is determined by the expression:

$$R_1 = 0.61\lambda/\theta_m. \tag{19}$$

and this parameter is considered as the ultimate resolution of an imaging optics based on an ideal lens using isotropic light emission from a point source. For the following it is more convenient to compare the different PSF characteristics based on the FWHM (full width at half maximum). For the Airy distributions presented in Fig. 13, the FWHM values are

$$FWHM(\theta_m = 0.1\ \text{rad};\ \lambda = 0.5\,\text{um}) = 2.57\,\text{um}. \tag{20}$$

Optics EXPRESS

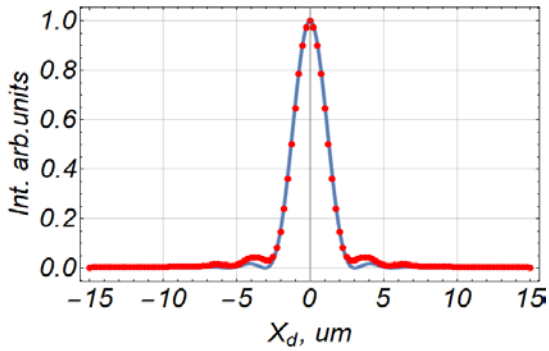

Fig. 13. Airy functions for $y_d = 0$; $\lambda = 0.5$ um; $\theta_m = 100/\gamma = 0.1\,\text{rad}$ (blue curve) and the PSF calculated for $\theta_{0x} = 110/\gamma$, $\theta_m = 100/\gamma = 0.1\,\text{rad}$, red dots (see Fig. 12).

For a Gaussian distribution the relation between σ and FWHM is FWHM = 2.36 σ. Applying this relation for the PSF for off-axis light collection (see Fig. 12) with σ_1 = 1.0 μm results in

$$FWHM(\theta_m = 0.1) = 2.36 \cdot 1.0 = 2.36\,\text{um} = 0.47\,\lambda/\theta_m. \qquad (21)$$

The position of the first minimum for the off-axis lens position amounts to 3.0 μm ($\lambda = 0.5$ um, $\theta_m = 0.1$) and can be compared directly to the first zero of the Airy distribution ($x_d = 3.05$ um, see Fig. 13). As conclusion, the spatial resolution of an OTR monitor with asymmetric light collection could be same as the one of a point source with isotropic light emission.

Figure 14 compares calculated OTR PSF functions for three different cases, (i) for standard imaging without using a mask (red line), (ii) for blocking the lens aperture by an asymmetric mask (blue line), and (iii) for off-axis light collection (green line). All PSF functions were calculated for the same set of parameters ($\gamma = 1000$, $\lambda = 0.5$ um, $\theta_m = 0.1$). As one can see from this comparison, the PSF for the off-axis light collection has the narrowest shape and possesses only a single maximum in contrast to the PSF for standard OTR imaging which exhibits a double-lobe shape. Calculating 2-D PSF functions for all cases one can estimate a total OTR intensity accepted by the aperture and for PSF functions presented in Fig. 14 ratio between such intensities is following: 1 (red line): 0.5 (blue line): 0.3 (green line).

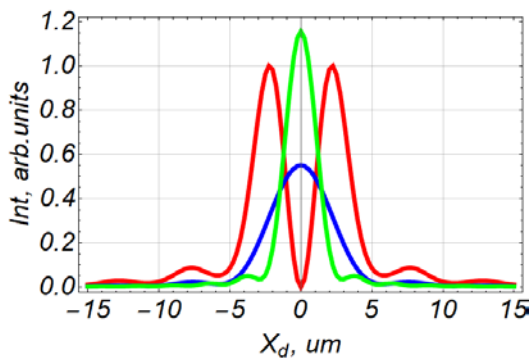

Fig. 14. Comparison of calculated OTR PSF functions for conventional light collection (red line), for 50% screening of the lens aperture (blue line) and for off-axis light collection (green line).

Optics EXPRESS

In order to reconstruct the shape of a micron or even sub-micron beam profile from a measurement based on OTR imaging, the usage of a PSF having a single maximum is a task which is much simpler than the approach which was developed in [16,17]. The authors of the work [17] used a conventional OTR monitor scheme with a lens diameter of 30 mm and a focal distance of 120 mm together with a polarizer and an optical bandpass filter (λ = 550 nm). The double-lobe distribution of the vertical polarization component was measured, possessing an inter-peak distance of about 10 μm. In the so-called "PSF dominated regime" an rms beam size could be extracted using a complicated algorithm including a self-calibration procedure. As a result they have obtained a minimum vertical beam size of 0.75 ± 0.03 μm [17]. In the view of the authors of the present work, the approach presented here will provide the same accuracy but an easier and more direct reconstruction procedure simply by determining rms sizes from the measured image and taking into account the calculated OTR PSF.

In the discussion so far it was assumed that the OTR PSF is the same for all beam electrons. Therefore, the beam image can be constructed from the convolution of the PSF with the beam distribution. In reality however, electrons emitting backward OTR have a certain transverse offset of about σ_x, σ_y with respect to the beam axis (which coincides with the optical axis in the presented scheme), and their field has to be calculated according to Eq. (2) while performing the integration and taking into account this offset. Especially in the case of asymmetric light collection schemes this might result in OTR PSFs which depend on the transverse particle position in the beam cross section such that the convolution argument for beam image construction is no longer valid. For the conditions under consideration however (σ_x, $\sigma_y \le 5$ um, $a =$ 500 mm) the argument of the MacDonald function in Eq. (2) is changed within a range of 10^{-2}, and the phase change there is even much smaller (in the order of 10^{-4}). As consequence it is expected that the PSF distortion due to a transverse offset will be smaller than a few percent and therefore can be neglected.

It was shown before that asymmetric optical schemes for OTR light collection can provide a significant narrowing of the OTR PSF distribution. Drawback of asymmetric OTR observation geometries however is a decrease in the overall intensity. In the ultra-relativistic approximation (which is valid for $\gamma \ge$ 1000 with accuracy better than 1%) it is possible to estimate the OTR photon yield for the cases under consideration using the formula

$$\Delta N_{ph} = \frac{\alpha}{\pi^2}\frac{\Delta\lambda}{\lambda}\int_{\Delta\Omega}\frac{\theta_x^2+\theta_y^2}{\left(\gamma^{-2}+\theta_x^2+\theta_y^2\right)}d\theta_x d\theta_y. \qquad (22)$$

In the following the yield of the OTR horizontal polarization component is estimated (which is described by the first term in the nominator in Eq. (13). For the shielding geometry presented in Fig. 6(f) and an optical bandpass filter with $\Delta\lambda/\lambda = 5\,\%$, the photon yield amounts to $\Delta N_{ph} \approx 2.4\cdot 10^{-4}\,\mathrm{ph}/e^-$. This corresponds to an intensity level of about 25% of the unpolarized OTR using a conventional imaging scheme without screening. Performing the similar calculation for the case of asymmetric light collection and a rotation of the lens optical axis at an angle of $110\,\gamma^{-1}$ and the same aperture, one obtains

$$\Delta N_{ph} \approx 1.4\cdot 10^{-4}\,\mathrm{ph}/e^-\,(\theta_m = 100/\gamma). \qquad (23)$$

The reduction of the OTR photon yield due to asymmetric light collection schemes will impose only minor restrictions: with the usage of a standard industrial camera for beam imaging based e.g. on the Sony IMX264 CMOS sensor [20] which has a dark noise of two electrons and a quantum efficiency of 68% at λ = 545nm, a single bunch current of 100 pC is sufficient in order to measure a single shot beam image, assuming (i) a Gaussian beam profile is sampled with 10 pixels per 1σ-width, (ii) in the central region of ± $2\sigma_{x,y}$ the number

of photons is well above the camera noise level, and (iii) the conversion between electrons and photons is determined according to Eq. (23). Using a scientific grade camera, single shot beam imaging with even smaller bunch currents will be possible.

6. Conclusion

It was shown that asymmetric optical schemes for OTR light collection can provide a significant narrowing of the OTR PSF distribution. The achieved spatial distribution with such a scheme can be close to the ultimate resolution of a point source described by the Airy disk, and the FWHM value is even smaller than λ / θ_m .

The calculations were carried out under the assumption of an ideal imaging lens, i.e. not taking into account optical imperfections as aberrations which might disturb the achieved resolution especially in the case of off-axis light collection. However, the consideration of higher order optical imperfections was out of focus of the present work. To the authors opinion these effects could be compensated in an experimental setup with a dedicated image lens design, e.g. by using aspheric lenses.

Drawback of asymmetric OTR observation geometries however is a decrease in the overall intensity. As it was shown before, the OTR intensity in this case is sufficient to allow single shot beam profile diagnostics with bunch charges down to 100 pC using standard cameras for industrial machine vision applications, in case of scientific grade cameras the sensitivity can even be increased. As consequence, the detectable OTR intensity will be well above the sensitivity threshold of a standard OTR monitor.

In order to further increase the sensitivity to a level of sub-micron spatial resolution [18], the techniques proposed in the present work could in principle be combined with detection schemes at smaller wavelengths using OTR in the UV and EUV spectral region [19].

Funding

Russian Ministry of Education and Science “Nauka” (3.1903.2017).

References

1. L. Wartski, S. Roland, J. Lasalle, M. Bolore and G. Filippi, “Interference phenomenon in optical transition radiation and its application to particle beam diagnostics and multiple-scattering measurements,” J. Appl. Phys. **46**(8), 3644–3653 (1975).
2. A. H. Lumpkin, B. X. Yang, W. J. Berg, M. White, J. W. Lewellen, and S. V. Milton, “Optical techniques for electron-beam characterizations on the APS SASE FEL project,” Nucl. Instrum. Meth. Phys. Res. A **429**(1-3), 336–340 (1999).
3. M. Ross, S. Anderson, J. Frisch, K. Jobe, D. McCormick, B. McKee, J. Nelson, T. Smith, H. Hayano, T. Naito, and N. Terunuma, “High resolution optical transition radiation beam profile monitor,” in Proceedings of Beam Instrumentation Workshop BIW 02, Upton (New York), AIP Conf. Proc., **648**, 237 (2002).
4. M. Borland, Y. C. Chae, P. Emma, J. W. Lewellen, V. Bharadwaj, W. M. Fawley, P. Krejcik, C. Limborg, S. V. Milton, H. D. Nuhn, R. Soliday, and M. Woodley, “Start-to-end simulation of selfamplified spontaneous emission free electron lasers from the gun through the undulator,” Nucl. Instrum. Meth. A **483**(1-2), 268–272 (2002).
5. E. Saldin, E. A. Schneidmiller, and M. V. Yurkov, “Klystron instability of a relativistic electron beam in a bunch compressor,” Nucl. Instrum. Meth. A **490**(1-2), 1–8 (2002).
6. M. Castellano and V. Verzilov, “Spatial resolution in optical transition radiation beam diagnostics,” Phys. Rev. STAB **1**, 062801 (1998).
7. A. P. Potylitsyn, “Image of optical diffraction radiation (ODR) source and spatial resolution of ODR beam profile monitor,”Advanced Radiation Sources and Applications, NATO Science Series II: Mathematics, Physics and Chemistry, Springer, N. Y **199**, 149–163 (2006).
8. G. Kube, “Imaging with optical transition radiation, transverse beam diagnostics for the XFEL,” Report No. TESLA-FEL, (2008).
9. M. L. Ter-Mikaelyan, *High Energy Electromagnetic Processes Condensed Media* (Wiley).
10. V. A. Verzilov, “Transition radiation in the pre-wave zone,” Phys. Lett. A **273**(1-2), 135–140 (2000), doi:10.1016/S0375-9601(00)00486-2.
11. P. Karataev, S. Araki, A. Aryshev, G. Naumenko, A. Potylitsyn, N. Terunuma, and J. Urakawa, “Experimental observation and investigation of the prewave zone effect in optical diffraction radiation,” Phys. Rev. STAB **11**, 032804 (2008).

Optics EXPRESS

12. F. G. Bisesto, M. Castellano, E. Chiadroni, and A. Cianchi, "Zemax simulations describing collective effects in transition and diffraction radiation," Opt. Express **26**(4), 5075–5082 (2018).
13. L. G. Sukhikh, G. Kube, and A. P. Potylitsyn, "Simulation of transition radiation based beam imaging from tilted targets," Phys. Rev. Accel. Beams **20**(3), 032802 (2017).
14. X. Artru, R. Chehab, K. Honkavaara, and A. Variola, "Resolution power of optical transition radiation. Theoretical considerations," Nucl. Instrum. Meth. B **145**(1-2), 160–168 (1998).
15. M. Born and E. Wolf, *Principles of Optic*s (Pergamon Press Ltd).
16. P. Karataev, A. Aryshev, S. Boogert, D. Howell, N. Terunuma, and J. Urakawa, "First observation of the point spread function of optical transition radiation," Phys. Rev. Lett. **107**(17), 174801 (2011).
17. K. Kruchinin, A. Aryshev, P. Karataev, B. Bolzon, T. Lefevre, S. Mazzoni, M. Shevelev, S. T. Boogert, L. J. Nevay, N. Terunuma, and J. Urakawa, "Sub-micrometer transverse beam size diagnostics using optical transition radiation," J. Phys. Conf. Ser. **517**, 012011 (2014).
18. M. V. Tsarev and P. Baum, "Characterization of non-relativistic attosecond electron pulses by transition radiation from tilted surfaces," New J. Phys. **20**(3), 033002 (2018).
19. L. G. Sukhikh, G. Kube, S. Bajt, W. Lauth, Yu. A. Popov, and A. P. Potylitsyn, "Backward transition radiation in the extreme ultraviolet region as a tool for the transverse beam profile diagnostics," Phys. Rev. STAB **17**, 112805 (2014).
20. https://www.sony-semicon.co.jp/products_en/IS/sensor0/industry/products/industry.html.